Sentinel-MSI and Landsat-OLI Data Quality Characterization for High Temporal Frequency Monitoring of Soil Salinity Dynamic in an Arid Landscape

Abdou Bannari ⬤, Nadir Hameid Mohamed Musa, Abdelgadir Abuelgasim, and Ali El-Battay

Abstract—Although the Sentinel-MSI and Landsat-OLI are designed to be similar, they have different spectral, spatial and radiometric resolutions. In addition, relative spectral response profiles characterizing the filters responsivities of the both instruments are not identical between the homologous bands. This paper analyse the difference between the reflectance in the homologous spectral bands of MSI and OLI sensors, VNIR and SWIR, for high temporal frequency monitoring of soil salinity dynamic in an arid landscapes. In addition, their conversion in term of Soil Salinity and Sodicity Index (SSSI) and in term of Semi-Empirical Predictive Model (SEPM) for soil salinity mapping were compared. To achieve these, analyses were performed on simulated data and on two pairs of images (MSI and OLI) acquired over the same area in July 2015 and August 2017 with one day difference between each pair. The results obtained demonstrate that the statistical fits between SMI and OLI simulated reflectance over a wide range of soil samples with different salinity degrees reveals an excellent linear relationship (R^2 of 0.99) for all bands, as well as for SSSI and SEPM. The Root Mean Square Difference (RMSD) values are null between the NIR and SWIR homologous bands, and are insignificant for the other bands. Moreover, the SSSI show an RMSD of 0.0007 and the SEPM express an excellent RMSD around 0.5 dS.m^{-1} reflecting a relative error between 0.001 and 0.05 for non-saline and extreme salinity classes, respectively. Likewise, the two used pairs of images exhibited very significant fits ($R^2 \geq 0.93$) for spectral band reflectance's, as well for SSSI and SEPM, yielding a RMSD values less than 0.029 for bands and less than 0.004 for SSSI. While, for SEPM, the RMSD fluctuate between 0.12 and 2.65 dS.m^{-1}, respectively, of non-saline and extreme salinity classes. Accordingly, we can conclude that the MSI and OLI sensors can be used jointly to monitor accurately the soil salinity and it's dynamic in time and space in arid landscape, provided that rigorous preprocessing issues must be addressed before.

Abdou Bannari is with the Space Pix-Map International Inc., Gatineau J8R 3R7, QC, Canada (e-mail: abannari@agu.edu.bh).

Nadir Hameid Mohamed Musa is with the Department of Geoinformatics, College of Graduate Studies, Arabian Gulf University, Manama 26671, Kingdom of Bahrain (e-mail: nadir@agu.edu.bh).

Abdelgadir Abuelgasim is with the Department of Geography and Urban Sustainability, United Arab Emirates University, A.-Ain 15551, United Arab Emirates (e-mail: a.abuelgasim@uaeu.ac.ae).

Ali El-Battay is with the International Center for Biosaline Agriculture, Dubai, United Arab Emirates (e-mail: a.elbattay@biosaline.org.ae).

Index Terms—Arid landscape, images data, landsat-OLI, semi-empirical model, sentinel-MSI, simulated data, soil salinity, soil salinity and sodicity index (SSSI), spectroradiometric measurements.

I. INTRODUCTION

ARID landscapes are seriously facing challenge of spatial and temporal distribution of soil salinity, particularly during drought periods [1], due to water quality and scarcity, the high temperature and the increased evapotranspiration rate [2]. In addition to water stress, these landscapes are vulnerable to salinization, marginality, and desertification as a consequence of human activities [3] and global climate change impact [4]. Obviously, these factors have significant impacts on land degradation, crop production, food security, economic aspects and infrastructure; as well as ecosystem functionality, human well-being, and sustainable development [5]. Around the world, soil salinity affect approximately 40% to 45% of the Earth land, especially in semi-arid and arid landscapes [6], and the global cost of irrigation-induced salinity is estimated around 11 billion US$ a year [7]. To remedy this situation in vulnerable landscape to salinization, there are methods available to slow down the processes and, sometimes, even reverse them. However, remedial actions require reliable information to help set priorities and to choose the type of action that is most appropriate for a specific location. In affected areas, farmers, soil managers, scientists, and agricultural engineers need accurate and reliable information on the nature, extent, magnitude, severity, and spatial distribution of the salinity against which they could take appropriate measures [8].

Soil salinity monitoring in space and time is complicated by salinity's dynamic nature, due to the influence of management practices, water table depth, soil permeability, microtopography, water use, rainfall, and salinity of groundwater. When the need for repeated measurements in time is multiplied by the extensive requirements of a single sampling period, the expenditures of time and effort with conventional soil sampling procedures increase proportionately. In general, measuring electrical conductivity extracted from a saturated soil paste at the laboratory (EC_{-Lab}) is the most accurate method used for soil salinity mapping [9]. Unfortunately, this method is expensive

and time consuming, especially for regular monitoring over a long period, and for comparisons over large areas [10], [11]. During the last two decades, remote sensing technology and image processing methods have outperformed these conventional methods. Currently, new remote sensing satellite instruments measuring soil salinity, coupled with modeling, programming, and mapping in GIS environment have significantly improved the potential for soil salinity monitoring in space with a very high temporal frequency [12]–[16]. The main advantage of remote sensing is the ability to map large areas at a relatively low cost by collecting information at regular intervals; therefore, monitoring becomes easier. This allows not only for the appropriate remedial action to be taken, but also for the monitoring of the effectiveness of any ongoing remediation or preventative measures, which facilitate monitoring, management, and decision-making [17].

Furthermore, actually, the availability of the new generation of medium spatial resolution, such as multispectral instruments (MSI) on board Sentinel-2 satellites and Operational Land Imager (OLI) sensor installed on Landsat-8 platform, offers new opportunities for long-term high-temporal frequency for Earth surfaces' observation and monitoring [18]. The free-availability of their data significantly advances the virtual constellation paradigm for mid-resolutions land imaging [19]–[21]. Thanks to the improvement of their spectral, radiometric, and temporal resolutions, they can expand the range of their applications to several natural resources and environmental domains for monitoring, assessing, and investigating [22]. The orbits of the both satellites are designed to ensure a revisiting interval time of approximately less than 5 days [23], thereby substantially increasing monitoring capabilities of the Earth's surface and ecosystems [24]. Their spectral resolutions and configurations are designed in such a way that there is a significant match between the homologous spectral bands [24], [25]. However, depending on the spectral sensitivity of the target under investigation [26], sensor radiometric drift calibration [27], atmospheric corrections [28], surface reflectance anisotropy [29], and sensors co-registration [30], [31], it is plausible that the natural surface-reflectance between MSI and OLI may be different. In addition, the relative spectral response profiles characterizing the filters (spectral responsivities) of the both instruments are not identical between the homologous bands, so some differences are probably expected in the recorded land-surface reflectance values; therefore, their data cannot be reliably used together [32], [33]. Obviously, the importance of these differences depends on the application (spectral characteristics of the observed target) and on the approach adopted to perform time-series analyses, mapping or change detection exploiting both instruments [26]. For instance, it is plausible that the extraction of soil salinity information in time over arid landscape using surface reflectance, empirical, semi-empirical, and/or physical approaches, can affect the results comparison.

Likewise, in addition to the remote sensing sensors technology improvement and innovation, several image processing methods and models were developed and applied for soil salinity retrieval. Based on simulated data and satellite images acquired with several sensors (TM, ETM+, OLI, MSI, ALI EO-1, and WorldView-3), numerous studies revealed that spectral confusion occurs in the visible and near-infrared (VNIR) spectral domain between the salt crust and the artifacts of soil optical properties. While other studies have shown that the shortwave infrared (SWIR) spectral bands allows better discrimination among salt-affected soil classes. Shrestha [34] concluded that the SWIR bands were the most correlated with soil salinity. Bannari *et al.* [14], [35]–[37] found that the SWIR bands of ALI, OLI, SMI, and WV3 offers the best potential for soil salinity detection and discrimination. Considering different soil types and geographic locations, Leone *et al.* [38], Odeh and Onus [39], and Zhang *et al.* [40] demonstrated that the SWIR bands could be used for soil salinity estimation in agricultural fields better than other spectral domains. Chapman *et al.* [41] showed that the SWIR bands of TM provide excellent discrimination of evaporite mineral zones in salt flats. Drake [42] described the various absorption peaks of the salts found in evaporite minerals in the SWIR wavelengths. The study undertaken by Hawari [43] showed that the absorption features in SWIR bands are consistent with the detection of the gypsum, halite, calcium carbonate, and sodium bicarbonate. According to Nawar *et al.* [44], the SWIR bands of ASTER exhibited the highest contribution for soil salinity estimation. Moreover, another study [45] indicated that the SWIR bands of the ETM+ sensor increase the accuracy of the soil salinity prediction.

This article analyzes and compares the difference between land-surface reflectance in the homologous spectral bands of MSI and OLI sensors, VNIR and SWIR, for soil salinity dynamic monitoring in an arid landscape. In addition, comparisons were carried out in terms of conversion of these surface reflectance to the *Soil Salinity and Sodicity Index* (SSSI) and to the *Semi-Empirical Predictive Model* (SEPM) for salt-affected soil mapping.

II. MATERIAL AND METHOD

Fig. 1 illustrates the used methodology; which is structured in four steps exploiting two independent datasets: simulated and images data. For simulated data, a field campaign was organized and 160 soil samples were collected with various degrees of soil salinity classes (i.e., extreme, very high, high, moderate, and low) including non-saline soil samples. The bidirectional reflectance factor was measured above each soil sample in a Goniometric-Laboratory using an *Analytical Spectral Devices* (ASD) FieldSpec-4 high resolution (Hi-Res) spectroradiometer [46]. The required preprocessing steps to allow their meaningful and accurate use and comparison were then carried out. Indeed, all measured spectra were resampled and convolved in the solar-reflective spectral bands of Sentinel-MSI and Landsat-OLI sensors using the *Canadian Modified Simulation of a Satellite Signal in the Solar Spectrum* (CAM5S) [47] based on Herman radiative transfer code (RTC), and the relative spectral response profiles characterizing the filters of each instruments in the VNIR and SWIR bands. While the two pairs of images were acquired with Sentinel-MSI and Landsat-OLI sensors over the same study site in July 2015 and August 2017 with one day difference between each pair. They were not cloudy, or cirrus contaminated, and without shadow effects because topographic variations are absent in the study area. They were radiometrically and atmospherically corrected to transform them to the
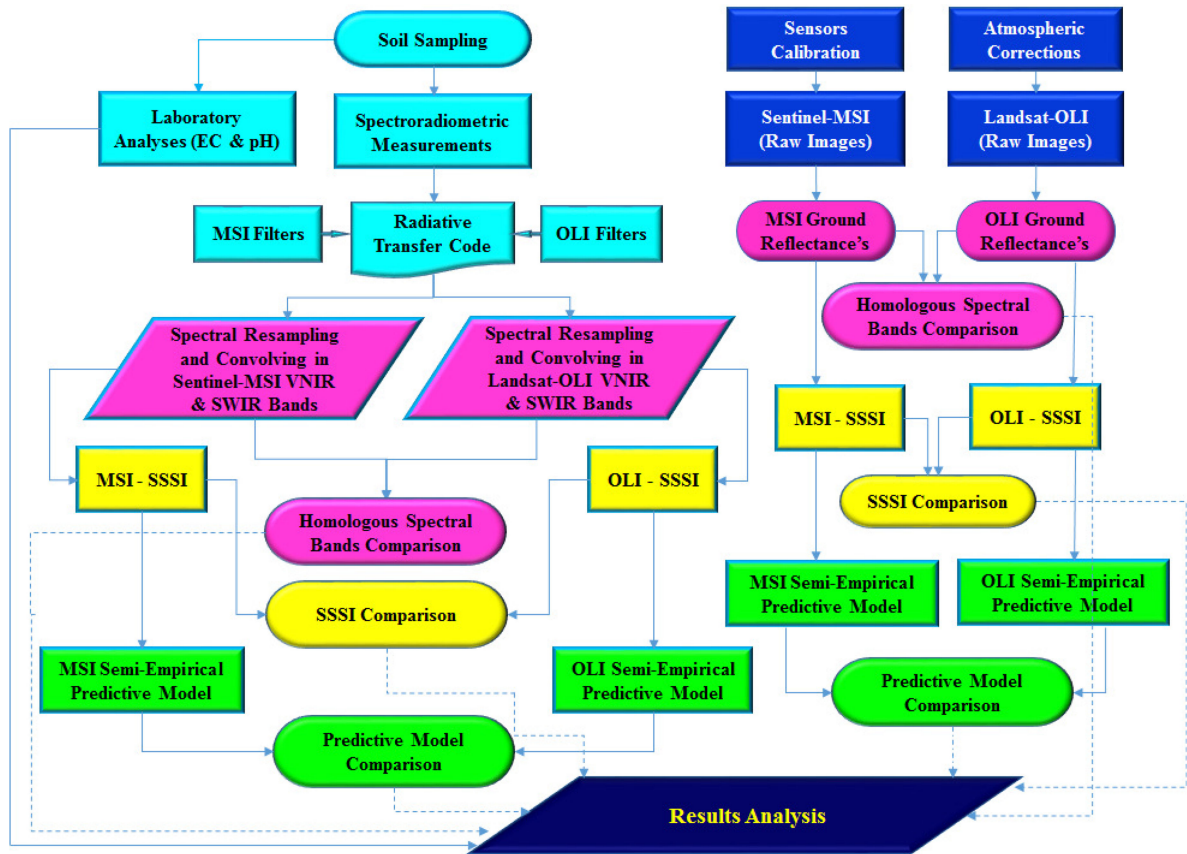
Fig. 1. Flowchart of the methodology.

ground surface reflectance, and the *Bidirectional Reflectance Distribution Function* (BRDF) were normalized to allow their meaningful comparison correctly. Finally, the standardized reflectance (simulated and images data) was converted in terms of SSSI and SEPM for soil salinity mapping. For comparison and sensor differences quantification, statistical fits were conducted using linear regression analysis ($p < 0.05$), coefficient of determination (R^2), and the *Root Mean Square Difference* (RMSD) was calculated. It is important to precise that subsequently to the spectroradiometric measurements, in the laboratory, soil chemical analyses (cations and anions: Ca^{2+}, Mg^{2+}, Na^+, K^+, Cl^-, and SO_4^{2-}), the soil reaction (pH) and the electrical conductivity (EC-$_{Lab}$) were extracted from a saturated soil paste, as well as the sodium adsorption ratio (SAR) being calculated [9]. These parameters provide reliable information about the degree of salinity in each considered soil sample, and thus help to understand the close relationship between the salt content values in each soil sample and its spectral behavior.

A. Study Site

The Kingdom of Bahrain ($25°32'$ and $26°00'$N, $50°20'$ and $50°50'$E) is an archipelago of 33 islands located in the Arabian Gulf, east of Saudi Arabia and west of Qatar (see Fig. 2) with a total land area of about 778.40 km^2. According to the aridity criteria and the great variations in climatic conditions, Bahrain

has an arid to extremely arid environment [48]. The climate is characterized by very high summer temperatures of an average 45 °C during June–September and an average of approximately 17 °C in winter from December–March. Rain is sparse, and occurs primarily from November to March, with an annual average of 72 mm, sufficient only to support the most drought-resistant desert vegetation. Mean annual relative humidity is over 70% due to the surrounding Arabian Gulf water, and the annual average potential evapotranspiration rate is 2099 mm [49]. Under such climatic conditions, where precipitation is excessively low to maintain a regular percolation of rainwater through the soil, soluble salts are accumulated in the soil, influencing soil properties and environment causing low soil productivity. Indeed, these factors have significant impacts on land degradation, crop production, economic aspects, and infrastructure, as well as ecosystem functionality, human wellbeing, and sustainable development [50]. Geologically, Bahrain is characterized by Eocene and Neocene rocks, which are partly covered by Quaternary sediments and a complex of Pleistocene deposits. The dominant rocks are limestone and dolomitic-limestone with subsidiary marls and shales. The leading structure is the north–south axis of the main dome, with minor cross-folds predominantly tilting from northeast to southwest. The beds are gently inclined towards the coast from the center of the main island. The fringes of Bahrain are covered by more recent marine and Aeolian sand dunes, which were derived from the Arabian land connection across the present Arabian Gulf.
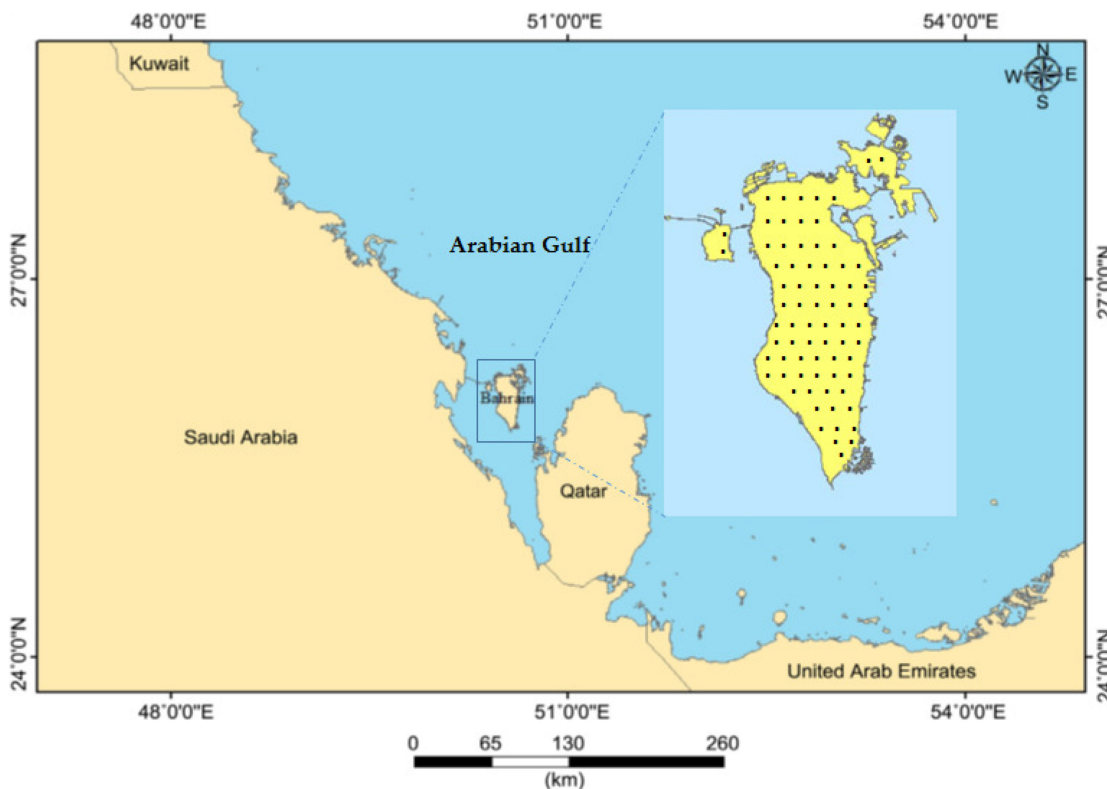
Fig. 2. Study site (Kingdom of Bahrain).

B. Soil Sampling and Laboratory Analyses

The soils of Bahrain are characterized by five different classes associated with moderate to shallow depths and are closely related to the terrain geology and geomorphology [51]. The natural Solonchak describes soils with no agricultural activities and retain a significant gypsum content (high and very high salinity). Then, there is the cultivated Solonchak soil class, which is located in areas either currently or previously exposed to agricultural activities. The Regosols soil class with moderate salinity is depicted as a mixture of raw minerals as well as the natural Solonchak soils, with the possibility for growing scattered halophytic plants. The miscellaneous land class that is represented by a composition of silts and fine sands with low salinity is suitable for agriculture. Finally, there is the non-saline soil class, which is imported to build artificial islands.

Based on Bahrain salt-affected soil map, six salinity classes are considered (see Fig. 3): extreme (class 1), very high (class 2), high (class 3), moderate (class 4), low (class 5), and non-saline (class 6). The extreme soil salinity class is characterized by the presence of high contents of soluble salts and the surface salt crust, which is sabkha (see C1 in Fig. 3). They are natural solonchaks soil (loamy and sandy, highly gypsiferous) devoid of any vegetation. The very high saline soils (class 2) are often encrusted with an efflorescence of salt crystals and a well-developed platy structure, which looks like the creation of a new sabkha (see C2 in Fig. 3). The high salinity soils (class 3) are composed of fine, white, sand-sized shell gravel and gravelly sand (see C3 in Fig. 3); the surface layers are sometimes

cemented by salt and are completely devoid of vegetation. The moderate soil salinity (class 4) is the dominant class in the southern half of Bahrain Island (see C4 in Fig. 3). It is calcareous to highly-calcareous, with calcium carbonate and dominated by shells and sand. Very sparse and scattered clumps of halophytic (salt-tolerant) plants are observed in this class area. Furthermore, in the northwest part of Bahrain Island we find the spatial distribution of low salinity soils (class 5), with acceptable fertility potential. This class is the only cultivated area in Bahrain (about 8% of the total area of the country), which is equipped with micro drip irrigation systems (see C5 in Fig. 3). Finally, the non-saline soil (class 6) describes accurately the man-made (artificial) infrastructure, industrial and urban zones (see C6 in Fig. 3).

A total of 160 samples were collected during a very dry period from Apr. 2 to 7, 2016, based on the spatial representativeness of the six major soil classes as discussed above. Samples were collected from the dry upper layer from 0 to 5 cm deep (crust) considering an area about 50×50 cm without vegetation residue (senescent or green) and moisture-free (see Fig. 3). Under the field conditions the soil moisture contents remained very low and not exceeded 0.08% in the all considered samples (loamy-sandy, silty-sandy, silty-clay-loam, highly gypsiferous), thus minimizing the impact of soil moisture on the measured spectra (see Fig. 4) [52], [53]. Moreover, observations and remarks about each sample (color, brightness, texture, etc.) were noted. The location of each point was automatically labeled and recorded using a 35 mm digital-camera equipped with a 28 mm lens and

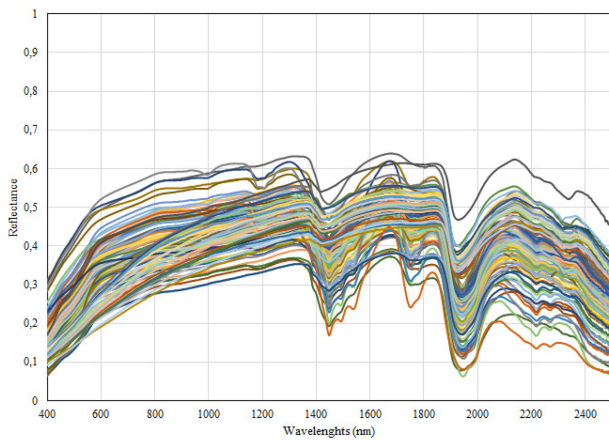Fig. 3. Photos of the six considered soil salinity classes (C1 to C6).

Fig. 4. Spectral signatures of 160 soil samples with different degrees of salinity.

accurate GPS survey ($\sigma \leq \pm 30$ cm) connected in real time to the GIS database.

After spectroradiometric measurements, which are described below, soil samples were crushed and then sieved to obtain the <2 mm fraction. Then, standard USDA laboratory methods and procedures [9] were used to measure the pH, the electrical conductivity (EC_{-Lab}), and the major soluble cations (Na^+, K^+, $Ca^{2+}+$, and Mg^{2+}) and anions (CO_3^{2-}, HCO_3^-, Cl^-, and SO_4^{2-}) using extraction from a saturated soil paste, and the SAR was also calculated [54]. In addition to the field observations, these parameters are considered in this study for the only purpose to provide reliable information about the degree of salinity content in each considered soil sample assisting the interpretation of spectroradiometric measurements and selected pixels from the used images.

C. Spectroradiometric Measurements

Spectroradiometric measurements were acquired in the Goniometric-Laboratory. The bidirectional reflectance spectra of soil samples were measured in air-dried conditions using an ASD (Analytical Spectral Devices Inc., Longmont, CO, USA) FieldSpec-4 Hi-Res (high resolution) spectroradiometer [46]. This instrument is equipped with two detectors operating in the VNIR and SWIR, between 350 and 2500 nm. It acquires a continuous spectrum with a 1.4 nm sampling interval from 350 to 1000 nm and a 2 nm interval from 1000 to 2500 nm. The ASD resamples the measurements in 1 nm intervals, which allows the acquisition of 2151 contiguous bands per spectrum. The sensor is characterized by the programming capacity of the integration time, which allows an increase of the signal-to-noise ratio (SNR), as well as stability. The data were acquired at nadir with a FOV of 25° and a solar zenith angle of approximately 5° by averaging 40 measurements. The ASD was installed at a height of 60 cm approximately over the target, which makes it possible to observe a surface of approximately 700 cm^2. A laser beam was used to coincide the center of the ASD-FOV with the center of the target under measurements. The reflectance factor of each soil sample (see Fig. 4) was calculated by rationing target radiance to the radiance obtained from a calibrated "spectralon panel" in accordance with the method described in Jackson *et al.* [55]. Corrections were made for the wavelength dependence and non-Lambertian behavior of the panel [56], [57].
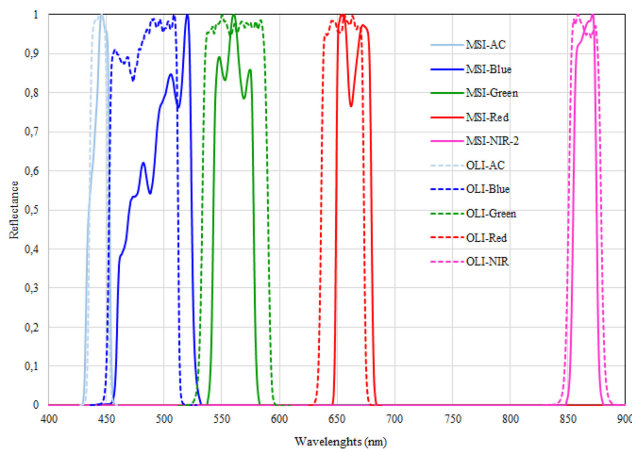
D. Sentinel-MSI and Landsat-OLI Simulated Data

The measured bidirectional reflectance factors using the ASD have a 1 nm interval, which allows the acquisition of 2151 contiguous hyperspectral bands per spectrum. However, most multispectral remote sensing sensors measured the reflectance that is
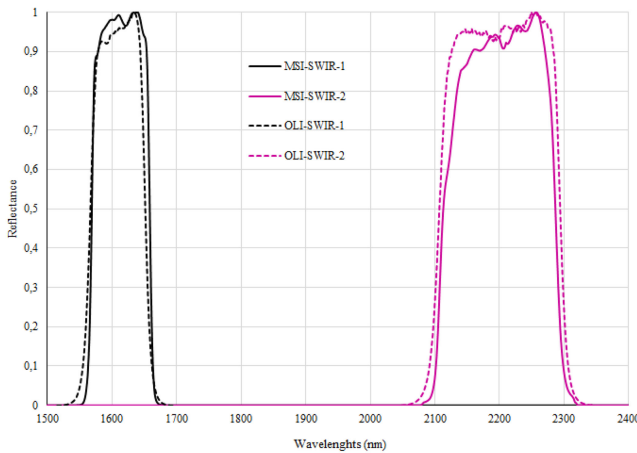
Spectral Bands	Sentinel-MSI					Landsat-OLI				
	λ Centre (nm)	$\Delta\lambda$ (nm)	Pixel Size (m)	SNR	$L_{ref}(\lambda)$ (w/m²/Sr/µm)	λ Centre (nm)	$\Delta\lambda$ (nm)	Pixel Size (m)	SNR	$E_0(\lambda)$ (w/m²/µm)
Coastal	443	20	60	129	129	443	16	30	130	1895.6
Blue	490	65	10	154	128	482	60	30	130	2004.6
Green	560	35	10	168	128	561	57	30	100	1820.7
Red	655	30	10	142	108	655	38	30	90	1549.4
NIR-1	865	20	20	72	52.5	865	28	30	90	951.2
SWIR-1	1609	85	20	100	4	1609	85	30	100	247.6
SWIR-2	2201	187	20	100	1.5	2201	187	30	100	85.5

λ = wavelength and SNR = signal to noise ratio.

Fig. 5. Sentinel-MSI and Landsat-OLI relative spectral response profiles characterizing the filters of each spectral band in the VNIR (a), and the SWIR (b).

integrated over broad bands. Consequently, the measured spectra of each soil sample was resampled and convolved to match the MSI and OLI solar-reflective spectral responses functions characteristics (see Fig. 5). In this step, the resampling procedure considers the nominal width of each spectral band (see Table I). Then, the convolution process was executed using the CAM5S

RTC [47]. This fundamental step simulates the signal received by the MSI and OLI sensors at the top of the atmosphere from a surface reflecting solar and sky irradiance at sea level considering the filters responsivities of individual sensor band (see Fig. 5), and assuming ideal atmospheric conditions without scattering and without absorption [58]–[61]. To understand correctly gain insights into any reflectance differences between the two sensors due to only their spectral responses functions differences, the 160 simulated sensor reflectance values were generated with various salinity degrees. These simulated reflectances in the VNIR and SWIR spectral band were fitted between MSI and OLI homologous bands using regression analysis ($p < 0.05$). This statistical examination step was used to evaluate the strength of the relationship between the reflectance information in homologous spectral bands, and the possibility to involve the both sensors together for salt-affected soil monitoring in time. It is important to note that the MSI-NIR-2 broad band (band-8: 785–900 nm) is not considered in this study because it is not a real homologous band of OLI-NIR, and it has a greatest reflective band difference with the OLI-NIR (851–879 nm). In fact, the OLI-NIR spectral response function intersects with only 20% of the MSI-NIR-2 response function. Moreover, the MSI red-edge bands were not considered also as they are not acquired by the OLI sensor.

E. Sentinel-MSI and Landsat-OLI Images Data

The Sentinel-2 "A and B" satellites were launched, respectively, on June 23, 2015 and March 7, 2017 with the identical MSI sensors on board. They were proposed to provide continuity to the SPOT missions [24] and to improve the Landsat-OLI temporal frequency. In fact, the synergy between Sentinel-MSI (A and B) and Landsat-OLI significantly increase the temporal resolution for several environmental and natural resource applications, such as the vigor of vegetation cover, emergency management, soil salinity dynamics, water quality, and climate change impact analysis at local, regional, and global scales. Sentinel-MSI is the result of close collaboration between the European Space Agency, the European Commission, industry, service providers, and data users. The MSI images the Earth's surface reflectivity with a large FOV (20.6°) in 13 spectral bands, 4 bands with 10 m pixel size (blue, green, red, and NIR-1), 6
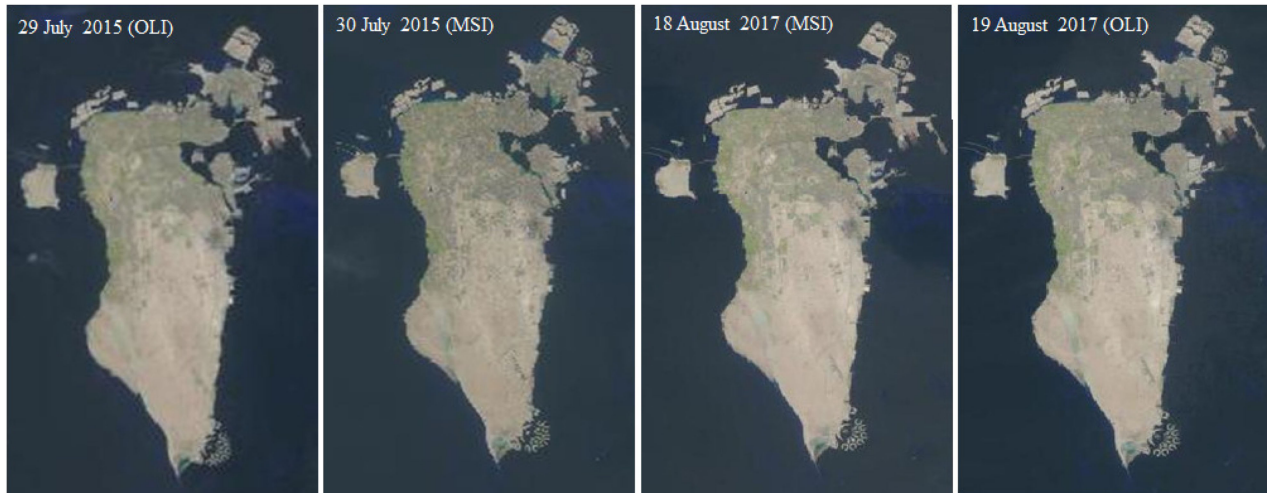
Fig. 6.   True color composite of raw OLI and MSI images data acquired over Kingdom of Bahrain in July 2015 (left) and August 2017 (right).

bands with 20 m (Red-Edge, NIR-2, and SWIR), and 3 bands with 60 m bands (coastal, water vapor, and cirrus). The swath of each scene is 290 km, permitting global coverage of the Earth's surface every 10 days. The MSI radiometric performance is coded in 12 bits, enabling the image acquisition in 4095 digital numbers, ensuring radiometric accuracy of less than 3% and an excellent SNR [27], [62]. The geometric registration precision is better than 0.15 pixels, and it was shown that no visual obvious misregistration was observed when the multitemporal MSI data were used [31]). Table I summarizes the effective bandwidth characteristics for MSI.

Furthermore, since 1972, the Landsat scientific collaboration program between the NASA and USGS constitute the continuous record of the Earth's surface reflectivity from space. Indeed, the Landsat satellites series support nearly five decades of a global moderate resolution data collection, distribution and archive of the Earth's continental surfaces [63], [64] to support research, applications, and climate change impact analysis at the global, the regional, and the local scales [19], [65], [66]. In February 11, 2013, the polar-orbiting Landsat-8 satellite was launched, transporting two push-broom instruments: OLI and TIRS. The OLI sensor collects land-surface reflectivity in the VNIR, SWIR, and panchromatic wavelength with a FOV of 15° covering a swath of 185 km with 16 days' time repetition at the equator. The band passes are narrower in order to minimize atmospheric absorption features [67], especially the NIR spectral band (0.865 μm). Two new spectral bands have been added: a deep blue visible shorter wavelength (band 1: 0.433–0.453 μm) designed specifically for water resources and coastal zone investigation, and a new SWIR band (9: 1.360–1.390 μm) for the detection of cirrus clouds. Moreover, the OLI design results in a more sensitive instrument with a significant amelioration of the SNR radiometric performance quantized over a 12-bit dynamic range (Level 1 data), raw data are delivered in 16 bit. This SNR performance and improved radiometric resolution provide a superior dynamic range and reduce saturation problems associated with globally maximizing the range of land-surface spectral radiance and, consequently, enable better

characterization of land-cover conditions [68], [45]. According to Gascon *et al.* [69], [46] and Markham *et al.* [27], Landsat-OLI and Sentinel-MSI on orbit reflective wavelength calibration is better than 3%. From geometric point of view, Stumpf *et al.* [70], [47] obtained a co-registration accuracy between images provided by both missions around $\pm$ 3 m by reference to accurate ground control point's measurements. Table I summarizes the effective bandwidth characteristics for OLI. In this research, two pairs of images data were used. They were acquired during the hottest period in the Middle-East with temperatures around 46–48°C. They were not cloudy and not contaminated with cirrus, without significant topographic variations and, consequently, the shadow effects were absent in the study area. The first pair was acquired with one day difference, the July 29 and July 30 2015 for OLI and MSI, respectively. The second pair was also recorded with one day difference on August 18 and August 19, 2017, respectively, for MSI and OLI (see Fig. 6). This very short time between each pair (MSI and OLI) data acquisition is so important to minimize the impact of land-use and soil surface conditions changes between these sensor observations.

F. Images Data Preprocessing

Prior to launch, the sensors are subject to rigorous radiometric and spectral characterization and calibration. However, post-launch absolute calibration is an important step to establish the relationship between at-sensor radiance and the digital number output for each pixel in the different spectral bands. Sensor radiometric calibration and atmospheric corrections (scattering and absorption) are fundamental preprocessing operations to restore the images radiometric quality at the ground level. The changes caused by these artifacts can be mistakenly attributed to changes in the land use and ground bio-physiological components, and errors can propagate in all subsequent image processing steps, such as spectral indices calculations, multitemporal analysis, climate change modeling, etc. [71], [72]. For converting the measured digital numbers by MSI and OLI sensors to the apparent radiance, the values of the solar zenith angle and rescaling

TABLE II
INPUT PARAMETERS FOR THE CAM5S RTC

Parameters	MSI Images	OLI Images
Terrain elevation (ASL)	0.755 km	
Sensor elevation	786 km	705 km
Date of over-flight	30 July 2015	29 July 2015
Time of over-flight (GMT)	10:22:47	10:04:19
Solar zenith angle (deg.)	20.201	23.811
Solar azimuth angle (deg.)	106.636	102.523
Date of over-flight	18 August 2017	19 August 2017
Time of over-flight (GMT)	10:20:33	10:04:46
Solar zenith angle (deg.)	22.516	26.010
Solar azimuth angle (deg.)	120.673	116.252
Atmospheric model	Mid-latitude Summer	
Aerosol model	Continental	
Horizontal visibility	50 km	50 km
Ozone content	0.319 cm-atm	
Water vapour	2.93 g/cm^2	
CO_2 mixing ratio	357.5 ppm (as per model)	

Note: ASL: Above Sea Level; GMT: Greenwich Mean Time; ppm: parts per million.

coefficients (gain and offset) delivered by USGS-EROS and ESA centers were used. Moreover, the CAM5S RTC [47] was used for atmospheric conditions simulation to calculate all the requested atmospheric correction parameters for MSI and OLI spectral bands. This RTC simulates the signal measured at the TOA from the Earth's surface reflecting solar and sky irradiance at sea level, while considering the sensors characteristics, such as the band passes of the solar-reflective spectral bands (see Fig. 5), satellite altitude, atmospheric condition, atmospheric model, Sun and sensor geometry, and terrain elevation. Consequently, all the requested atmospheric correction parameters were calculated and applied to transform the apparent reflectance at the TOA to the ground reflectance. Table II summarizes the input parameters for the CAM5S RTC for each pair of images. To preserve the radiometric integrity of the images, absolute radiometric calibration and atmospheric effects corrections were combined and corrected in one step [73] to generate ground surface reflectance images using the Canadian image processing system PCI-Geomatica.

Furthermore, knowing that Earth's natural surfaces do not have a Lambertian spectral behavior, because both solar and observing zenith angles exert a radiometric distortion impact on surfaces reflectance, the BRDF problem was normalized. According to Roy *et al.* [66] along the Landsat-OLI bands (edges by reference to the image center) the reflectance can vary by less than 6% due to this BRDF effects. Moreover, Roy *et al.* [29] reported that this problem can affect the Sentinel-MSI bands by approximately 8% because of its large FOV. Certainly, these differences may constitute a source of errors for biophysical and physiological parameters extraction, as well as for general remote sensing applications because their values as mentioned

before are relatively more meaningful than the sensor calibration errors [27] and atmospheric corrections [69]. To normalize the BRDF influence on the ground surface reflectance images of MSI and OLI, a semi-empirical approach [74] was applied in this research.

G. Data Conversion

For soil salinity detection and mapping, many soil salinity spectral indices and models have been proposed in the literature [75]–[78]. A comparative study among several semi-empirical predictive models based on salinity indices, such as *Brightness Index*, *Normalized Difference Salinity Index*, *Salinity Indices*, *ASTER Salinity Index*, SSSI, etc., was achieved for accurate salt-affected detection in irrigated agricultural land (slight and moderate salinity classes) in North Africa and in the arid landscape (slight, moderate, strong, and very strong salinity classes) in Middle-East [36], [79], [80]. The results of these studies showed that the SEPM model based on SSSI, which integrate the SWIR bands, provided the best accuracy for salt-affected soil classes' detection and mapping. Consequently, in this study, the comparisons of SSSI and SEPM are undertaken in the same way as surface reflectance derived from simulated and images data to quantify the impact differences between relative spectral response profiles characterizing the filters of homologous bands of MSI and OLI sensors. The SSSI and SEPM equations are as follows [35], [36]:

$$\text{EC}-_{\text{Predicted}} = C^{\text{ste}}. \left[4521.(\text{SSSI})^2 + 125.(\text{SSSI}) + 0.41 \right] \tag{1}$$

$$\text{SSSI} = (\rho_{\text{SWIR}-1}.\rho_{\text{SWIR}-2} - \rho_{\text{SWIR}-2}.\rho_{\text{SWIR}-2})/(\rho_{\text{SWIR}-1}) \tag{2}$$

where

EC-$_{\text{Predicted}}$ SEPM;
$\rho_{\text{SWIR-1}}$ Reflectance in MSI and OLI SWIR-1 channel;
$\rho_{\text{SWIR-2}}$ Reflectance in MSI and OLI SWIR-2 channel;
C$^{\text{st}}$ Scaling factor, which theoretically enables an up-scaling between the spatial information measured in the field and its homologous information derived from the image [81].

However, in this study case its value is equal to one because we are comparing data from the same sources (MSI to OLI from simulated data, or image to image), and not from the field to the image.

H. Statistical Analyses

As discussed previously, the MSI and OLI relative spectral response profiles characterizing the filters of each spectral band are relatively different (see Fig. 5). To examine the impact of this difference, statistical analyses were computed using "Statistica" software considering simulated and images data. The relationships between derived product values (reflectance, SSSI, and SEPM) from MSI against those from OLI were analyzed using a linear regression model ($p < 0.05$). As well, the R^2 was used to evaluate the strength of this linear relationship. For this process, the resampled and convolved spectra of 160 soil samples and images ground reflectance data were used, and the homologous values in VNIR and SWIR bands of MSI and OLI were compared using the 1:1 line. Ideally, these independent variable values should have a correspondence of 1:1. Additionally, the RMSD between the both sensors was derived for simulated and images data as follows [21], [82]:

$$\text{RMSD} = \sqrt{\frac{\sum_i^n \left(v_i^{\text{OLI}} - v_i^{\text{MSI}}\right)^2}{n}} \tag{3}$$

where RMSD is the root mean square difference between corresponding Landsat-OLI and Sentinel-MSI variables values (reflectance, SSSI, and SEPM) derived from simulated spectra and images-pixels, v_i is the variable under analysis and "i" is the number of variable ($i = 1$ to n).

III. RESULTS ANALYSES

A. Soil Laboratory Analysis and Simulated Data Comparison

Fig. 4 shows that overall, the spectral signatures of the 160 considered soil samples are controlled by the type of salt existing in each soil sample, such as sulfates, chlorides, and/or carbonates. The results showed different amplitudes and several absorption features depending on the chemical compositions and the mineralogy of the existing salts in the selected soil samples. Moreover, the spectral signatures are also influenced by several factors, such as mineralogical composition, impurity, structure, and texture of the soil and salt crystals, and the soil optical properties (color brightness, and roughness), particularly in the VNIR spectral domain [14]. Furthermore, the laboratory analyses of all soil samples revealed that the moisture content values are distributed in a very limited range between 0% and

0.08%, thus minimizing the impact of moisture content on the measured spectra (see Fig. 4). In fact, only three weak absorption bands near 1350, 1800, and 2208 nm were observed in some samples (atmospheric water vapor absorption features at 1440 and 1920 nm are not considered in this analysis). While, the other absorption features are automatically linked to the salt mineralogy, particularly the gypsum, sodium, chloride, halite, calcium carbonate, and sodium bicarbonate, which reveals significant absorption features at 980, 1000, 1190, 1210, 1400, 1450, 1490, 1540, 1748, 1780, 1800, 1900, 1945, 1975, 2175, 2215, 2265, and 2496 nm [14]. These observations corroborate findings of other studies [14], [43], [53].

Otherwise, the major exchangeable cations and anions in the considered six soil sample classes (Ca^{2+}, Mg^{2+}, Na^+, K^+, Cl^- and SO_4^{2-}), pH, EC-$_{\text{Lab}}$, and SAR values were calculated from the sampling points representing each soil class separately and summarized in Table III. The laboratory analyses revealed a very high concentration of sodium (Na^+) and dominant chloride anion (Cl^-). Globally, the values of EC-$_{\text{Lab}}$, Na^+, and SAR increase gradually and very significantly from non-saline soil to extreme soil salinity (sabkha). Indeed, the non-saline and low soil salinity classes, which support the agricultural system in Bahrain, are characterized by low EC-$_{\text{Lab}}$ ($2.6 \leq$ EC-$_{\text{Lab}} \leq$ 4.4 dS.m^{-1}) and SAR (≤ 10.3). The moderate salinity class was characterized by EC-$_{\text{Lab}}$ around 7.4 dS.m^{-1}, and SAR nearby 12.7 representing the dominant soil class in Bahrain and is a part of the Regosols soil category that allows for the growth of halophytic plants. Contrariwise, the other three soil salinity classes with high, very high, and extreme salinity content showed exceptional EC ($67 \leq$ EC-$_{\text{Lab}} \leq 600$ dS.m^{-1}) and very high SAR (≥ 99.2) values. These three classes represent the natural Solonchak soil category. While, the pH values (7.1 to 8.6) are very informative as regards the preponderance of carbonate and the presence of bicarbonate in the soils which contribute significantly to the alkalinity aspect of the soil. Clearly, these results confirm our choice of different soil salinity classes that represent the truth of arid landscapes, which is fundamental for the analyses of the impact of the spectral response functions difference on the surface reflectance and the products derived from the homologous spectral bands (VNIR and SWIR) of the MSI and OLI sensors.

Fig. 7 illustrates the scatter plots of SMI and OLI simulated surface reflectance values at the top of the atmosphere, which were generated from 160 soil samples with unlike salinity degrees ($2.6 \leq$ EC-$_{\text{Lab}} \leq 600$ dS.m^{-1}) to analyze the impact of differences in reflectance exclusively due to dissimilarities in spectral response function between homologous spectral bands. These scatter plots reveals a very good linear relationship (R^2 of 0.999) between homologous bands whit the slopes and intercepts very near to unit and zero, respectively. Table IV summarizes the obtained regression fit equations, the coefficient of determination, and the RMSD between MSI and OLI simulated surface reflectance in the homologous bands, as well as the derived SSSI and SEPM products. The RMSD values are null between the NIR and SWIR homologous bands, and are insignificant for the other bands (i.e., 0.003 for coastal and 0.001 for the blue, green, and red bands). Highlighting the good behavior of SWIR

TABLE III
LABORATORY DETERMINATION OF PH, EC-$_{Lab}$ AND IONS CONTENT IN THE DIFFERENT SOIL SALINITY CLASSES

Salinity class	EC-$_{Lab}$ (dS.m^{-1})	pH	Ca^{2+}	K$^+$	Mg^{2+}	Na$^+$	Cl$^-$	SO$_4{}^{2-}$	SAR (mmoles/L)$^{0.5}$
					(mg.l^{-1})				
Extreme	507.0	7.6	1276	843	672.0	154700	170715	11275	874.0
V. high	170.0	7.2	1878	1454	2874.0	76373	100281	28020	258.9
High	67.0	7.5	1905	651	1581.0	24171	48546	5488	99.2
Moderate	7.4	8.6	531	67	181.0	1324	2480	881	12.7
Low	4.4	8.2	284	44	96.0	782	1329	754	10.3
Non-saline	2.6	7.9	154	28	58.4	530	886	63	9.2

TABLE IV
REGRESSION FIT EQUATIONS BETWEEN MSI AND OLI SIMULATED SURFACE REFLECTANCE IN THE HOMOLOGOUS SPECTRAL BANDS, AND THE DERIVED RMSD FOR SSSI AND SEPM

Spectral Bands	Regressions between simulated data in OLI and MSI bands		
	Regression coefficients	R^2	RMSD
Coastal	OLI = 1.0346 MSI + 0.0075	0.99	0.003
Blue	OLI = 0.9875 MSI - 0.0048	0.99	0.001
Green	OLI = 0.9979 MSI + 0.0003	1.00	0.001
Red	OLI = 1.0050 MSI - 0.0053	1.00	0.001
NIR-2	OLI = 1.0001 MSI - 0.0002	1.00	0.000
SWIR-1	OLI = 0.9992 MSI + 0.0007	1.00	0.000
SWIR-2	OLI = 0.9976 MSI - 0.0017	1.00	0.000
SSSI	OLI = 1.0139 MSI - 0.0027	1.00	0.0007
SEPM	OLI = 0.9948 MSI - 0.9648	1.00	0.003 to 0.553*

* dS.m^{-1} for electrical conductivity unite; 0.003 dS.m^{-1} for non-saline and 0.553 for extreme salinity classes.

bands, the calculated SSSI values fit perfectly with the line 1:1 (R^2 of 0.9996) showing a slope of 1.01, intercept of 0.002, and RMSD of 0.0007 (see Fig. 8). Moreover, independently to the degrees of salinity in the considered soil samples, the simulated SEPM values fit perfectly with 1:1 line expressing an excellent coefficient of determination (R^2 of 0.9994) and a slope near to the unit (0.995). The calculated RMSD for the SEPM vary between 0.003 and 0.5 dS.m^{-1} (electrical conductivity unit) reflecting a relative error that varies between 0.001 and 0.05 for salinity classes varying between 2.5 (non-saline) and 600 dS.m^{-1} (extreme salinity). Moreover, this difference is identical to the electrical conductivity accuracy measurement in the filed using electronical instruments [83]. These results pointed out that MSI and OLI sensors can be combined for high temporal frequency to monitor soil salinity dynamic in time and space in an arid landscape. However, it is important to remember that these simulations took place in a Goniometric-Laboratory using close range measurements protocol assuming indirectly that the measured surfaces are homogeneous with Lambertian reflectance (by reference to spectralan). In addition, the atmospheric scattering and absorption are absent, errors related to radiometric calibration and geometric location are also absent, no topographic variation, no residual clouds or shadows, and no BRDF impact. Evidently, these simulations in a controlled

environment are ideal comparatively to the real Earth observation conditions using images data acquired with MSI and OLI sensors and covering a large pixel surface (900 m^2) with mixed information.

B. Images Results Analysis

The spectral bands of MSI have unlike spatial resolutions (10, 20, and 60 m) than those of OLI bands (30 m). To handle this spatial difference and to generate data correspondingly to OLI images for analyses, MSI images were resampled automatically in 30 m pixel size considering UTM projection and WGS84 datum. Based on the measured GPS ($\sigma \pm 30$ cm) coordinates location, the considered 160 sampling points representing all salinity classes (approximately 26 pixels per class) were carefully located and selected from the homologous spectral bands in the booth pair of images. Then, comparisons of the surface reflectance, and derived SSSI and SEPM were undertaken in the same way as for the simulated data using regression analysis, R^2, and RMSD. Since the results obtained from the two pairs of images are similar (see Table V), only the results retrieved from the pair acquired in August 2017 are presented in Fig. 9. This scatter plots shows the relationship between surface reflectance in the VNIR and SWIR homologous bands of SMI and OLI
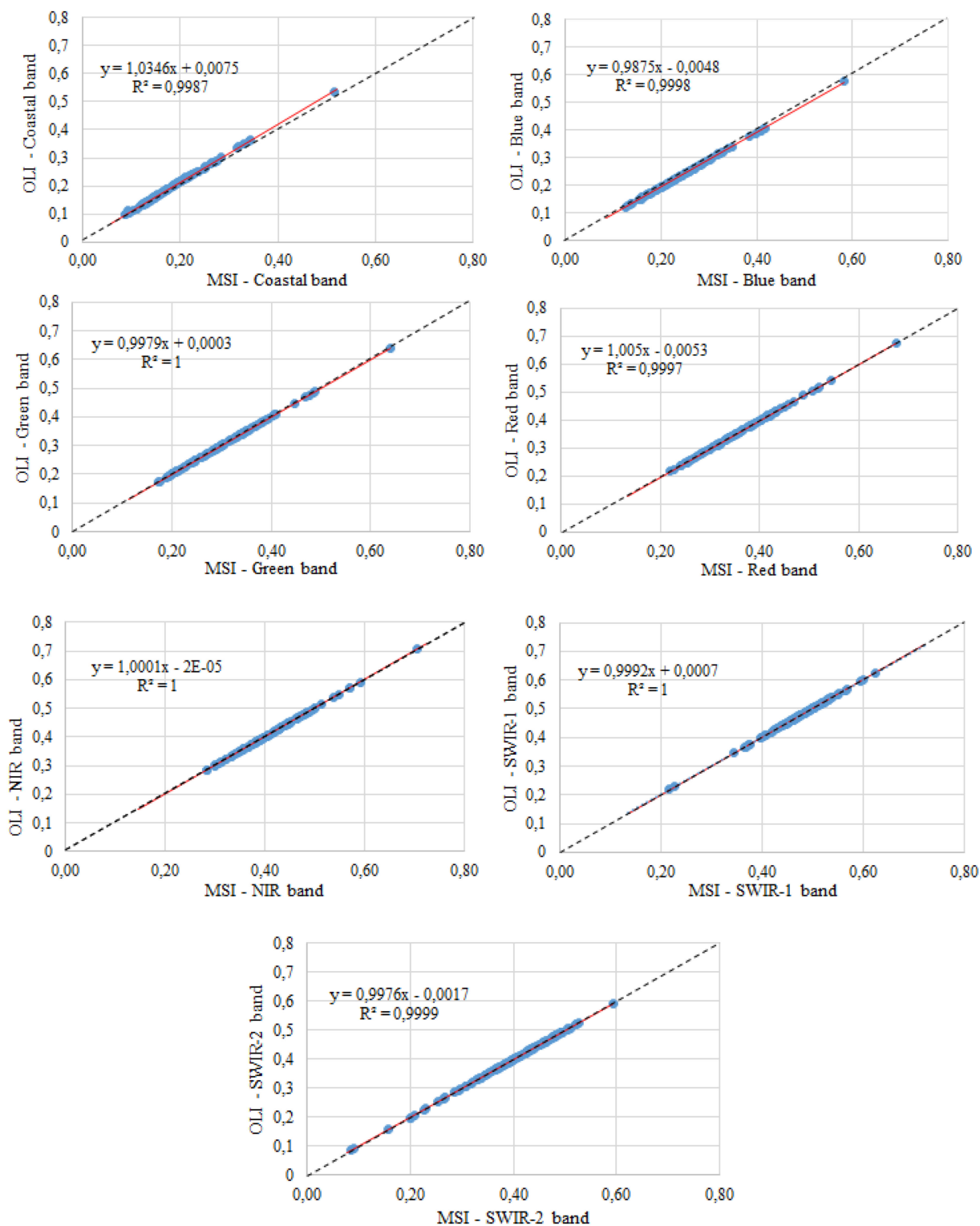
Fig. 7.   Compared surface reflectance simulated and convolved in Sentinel-MSI and Landsat-OLI homologous spectral bands.

sensors acquired over a wide range of soil samples with different salinity degrees ($2.6 \leq$ EC-$_{\text{Lab}} \leq 600$ dS.m^{-1}). A very good linear relationship between all homologous bands is observed with the slopes and intercepts near to unity and zero, respectively. The used images in each pair had very significant fits (R^2

≥ 0.96) for green, red, NIR, and SWIR homologous spectral bands (see Fig. 9 and Table V). For these bands, the majority of sampling points are located around the line 1:1. While, the coastal and blue bands fits with R^2 of 0.93 and 0.96, respectively. Although these last two bands depicts a good fit to the 1:1 line,
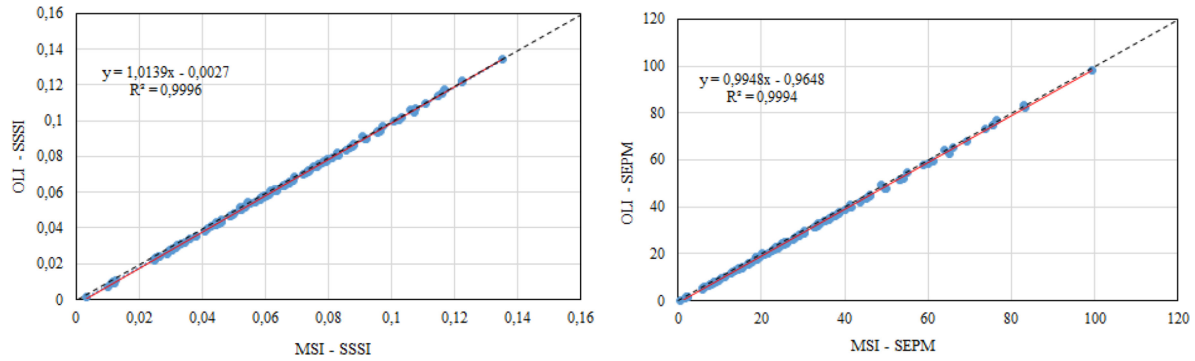
Fig. 8.   Compared SSSI (left) and SEPM (right) derived from Sentinel-MSI and Landsat-OLI simulated data.

TABLE V
REGRESSION FIT EQUATIONS BETWEEN MSI AND OLI IMAGE SURFACE REFLECTANCE IN THE HOMOLOGOUS SPECTRAL BANDS, AND THE DERIVED
RMSE FOR SSSI AND SEPM

	Regressions between OLI and MSI for 2015			Regressions between OLI and MSI for 2017		
	Equations	R^2	RMSD	Equations	R^2	RMSD
Coastal	OLI = 0.8097 MSI + 0.009	0.94	0.026	OLI = 1.1000 MSI + 0.050	0.93	0.029
Blue	OLI = 1.1000 MSI + 0.048	0.96	0.021	OLI = 1.0800 MSI + 0.040	0.96	0.021
Green	OLI = 0.9241 MSI + 0.008	0.96	0.015	OLI = 1.0400 MSI + 0.020	0.97	0.015
Red	OLI = 0.9643 MSI + 0.004	0.98	0.015	OLI = 0.9900 MSI + 0.010	0.98	0.011
NIR	OLI = 1.0197 MSI + 0.019	0.99	0.010	OLI = 1.0500 MSI + 0.020	0.98	0.009
SWIR-1	OLI = 0.9800 MSI + 0.000	0.99	0.010	OLI = 1.0300 MSI + 0.010	0.99	0.008
SWIR-2	OLI = 1.0000 MSI + 0.000	0.99	0.007	OLI = 1.0500 MSI + 0.020	0.99	0.008
SSSI	OLI = 0.9839 MSI + 0.003	0.97	0.006	OLI = 0.9700 MSI + 0.000	0.94	0.004
SEPM *	OLI = 0.9352 MSI + 0.912	0.96	0.12 to 1.98 *	OLI = 0.9700 MSI + 1.460	0.95	0.12 to 2.65 *

* dS.m^{-1} for electrical conductivity unite; 0.12 dS.m^{-1} for non-saline and 2.65 for extreme salinity classes.

in general the reflectance are relatively overestimated in MSI than in OLI. This is likely due to the correction of scattering effects by aerosols in these short wavelengths, as well as to the OLI medium spatial resolution compared to the original pixel size of MSI. These observations have been also noted in other studies [21]. Furthermore, the RMSD values are insignificant for the NIR and SWIR homologous bands (≤ 0.009), and are very small (≤ 0.029) in the visible bands (see Table V). Globally, the reflectance in OLI visible bands is slightly lower against those in MSI.

Fig. 10 illustrates the relationship between the derived SSSI and SEPM products from MSI and OLI data acquired in 2017. The SSSI values fit significantly with the line 1:1 (R^2 of 0.95) showing a slope of 0.97, intercept of 0.00, and RMSD of 0.004. Moreover, the predicted salinity values using the SEPM are fitting well with 1:1 line expressing an excellent coefficient of determination (R^2 of 0.95) between the derived information from the two sensors, with a slope of 0.97 (near to the unit) and intercept of 1.46. This scatter-plot showed also a relative underestimation of very high salinity class ($200 \leq$ EC-$_{\text{Lab}} \leq 600$ dS.m^{-1}) in the OLI SEPM than that of MSI. Whereas, the RMSD calculated for SEPM varied from 0.12 to 2.65 dS.m^{-1} for non-saline and extreme salinity classes, respectively. Almost similarly to simulated data, these RMSD reflect relative errors varying between 0.005 and 0.03 for the considered soil salinity classes ($2.6 \leq$ EC-$_{\text{Lab}} \leq 600$ dS.m^{-1}), which are quite identical

to the electrical conductivity accuracy measurements in the filed using electronical instruments [83]. The small RMSD values found between homologous bands of the two considered pair of images (MSI and OLI) and the derived SSSI and SEPM could not be attributed only to sensor spectral response function differences. Definitely, in addition to the unlike spatial resolutions and the resampling MSI pixels, these relative small differences are probably also due to the signal saturation, which resulted by the difference in radiometric resolutions between both sensors. This saturation may be more pronounced over bright and strongly reflective surfaces such as white salt-crust areas, especially when specular effect is strongly pronounced. It can also be magnified by the non-Lambertian surfaces that cause a non-negligible BRDF effects [29], as well as the BRDF standardization (FOV of $\pm 10.3°$ for MSI rather than $\pm 7.5°$ for OLI), which is based on a semi-empirical model [74]. Moreover, it can also be caused by the residual errors of sensor radiometric calibration and atmospheric corrections that are never perfect, particularly at shorter wavelengths, where atmospheric scattering impacts are usually greatest, and also because the images have not been atmospherically corrected pixel by pixel but rather band by band.

In general, independently to the used data (simulated or images) the statistical fits were found to be highly significant ($0.95 \leq R^2$) and the reached RMSD values (<0.029) were smaller than the accuracy of radiometric calibration process (0.03) as demonstrated by Markham *et al.* [7]. Moreover, despite the small
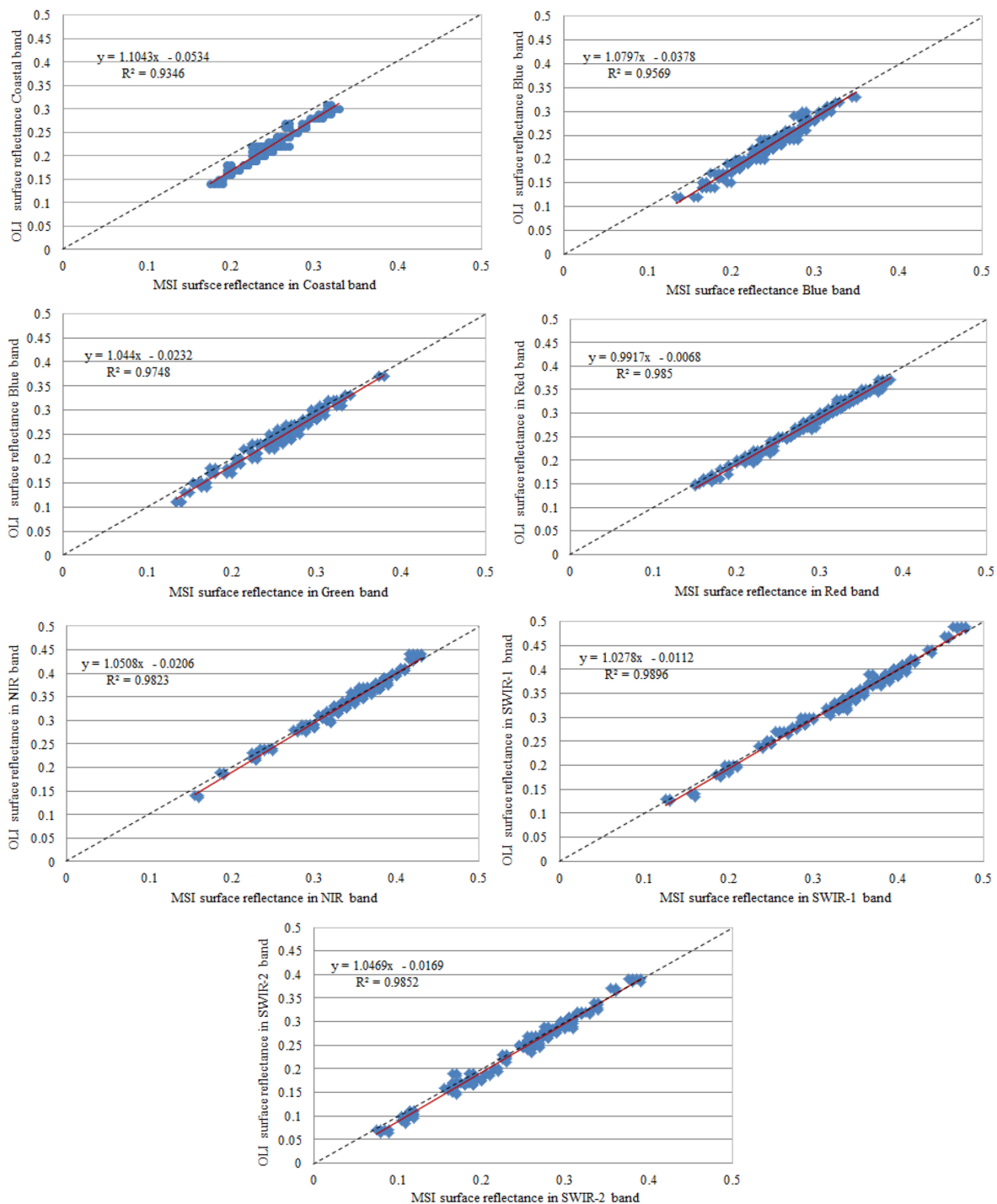
Fig. 9. Compared surface reflectance acquired with Sentinel-MSI and Landsat-OLI spectral bands (VNIR and SWIR) acquired on August 2017.

differences especially in coastal and blue bands, these results pointed out that MSI and OLI sensors can be combined for high temporal frequency to monitor soil salinity dynamic in time and space in an arid landscape. However, rigorous preprocessing issues (sensors calibration, atmospheric corrections, and BRDF normalization) must be addressed before the joint use of acquired data with these two sensors. This result corroborate the finding of Davis *et al.* [84], who have demonstrated that the two sensors have similar salinity modeling skill in Hyde County

areas in North Carolina (USA). Moreover, although this article is focusing specifically on soil salinity as a specific target, the results obtained are consistent with previous research projects considering several other applications around the world. For instance, comparing surface reflectance and derived biophysical variables over Australian territory, Flood [26] indicated good compatibility between SMI and OLI instruments with RMSD < 0.03 for surface reflectance in VNIR and SWIR bands, and an RMSD around 0.05 for biophysical variables. Pastick *et al.* [85]
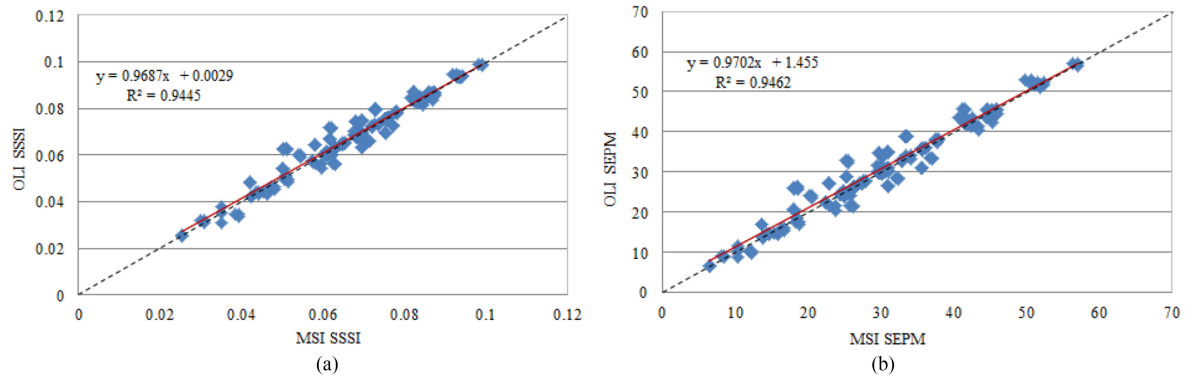
Fig. 10.   Compared SSSI (a) and SEPM (b) derived from Sentinel-MSI and Landsat-OLI images data acquired on August 2017.

demonstrated that observations made by MSI and OLI can be used to monitor land-surface phenology accurately in drylands of the Western United States. Vuolo *et al.* [86] compared surface reflectance and biophysical products of many targets over six test sites in Europe showed a good relationship between these two sensors products, yielding RMSD values around 0.03 reflectance units. Some tests performed on simulated data and on real images data acquired simultaneously with MSI and OLI over a wide variety of land cover types (agricultural fields, inland, and open shallow water) showed a very high coefficient of determination (R^2 of 0.98) between homologous bands [18]. Moreover, the comparison of an automated approach for burned areas mapping combining OLI and MSI data, preprocessed rigorously, showed that both sensors have identified similarly the spatial patterns for burned areas [87].

IV. CONCLUSION

The MSI onboard Sentinel satellites and the OLI installed on Landsat-8 satellite are designed to be similar in the perspective that their data be used together to support global Earth surface reflectance coverage for science and development applications at medium spatial resolution and near daily temporal resolution. However, relative spectral response profiles characterizing the filters responsivities of the both instruments are not identical between the homologous bands, so some differences are probably expected in the recorded land-surface reflectance values. This article analyzes and compares the difference between the reflectance of the homologous spectral bands in the VNIR and SWIR of MSI and OLI sensors for soil salinity dynamic monitoring in arid landscapes. In addition, comparisons were carried out in term of conversion of these surface reflectance to the SSSI and in term of the SEPM for salt-affected soil mapping. To achieve these, analyses were performed on simulated data and on two pairs of images acquired over the same area in July 2015 and August 2017 with one day difference between each pair. For simulated data, a field campaign was organized and 160 soil samples were collected with various degrees of soil salinity classes (i.e., extreme, very high, high, moderate, low, and non-saline). The bidirectional reflectance factor was measured above each soil sample in a Goniometric-Laboratory

using an ASD spectroradiometer. Then, these measurements were resampled and convolved in the solar-reflective bands of SMI and OLI using the CAM5S TRC and the relative spectral response profiles characterizing the filters of these instruments. Furthermore, the used pairs of images were not cloudy, or cirrus contaminated, and without shadow effects. They were radiometrically and atmospherically corrected, and the differences related to BRDF were normalized. To generate data for analysis, similarly to OLI, MSI images were resampled systematically in 30 by 30 m pixel size considering UTM projection and WGS84 datum. The comparisons of the surface reflectance, and derived SSSI and SEPM were undertaken in the same way for simulated and images data using regression analysis, R^2, and RMSD. The results obtained demonstrate that the statistical fits between SMI and OLI simulated surface reflectance over a wide range of soil samples with different salinity degrees reveals an excellent linear relationship (R^2 of 0.99) for all bands, as well as for SSSI and SEPM. The RMSD values are null between the NIR and SWIR homologous bands, and are insignificant for the other bands (i.e., 0.003 for coastal and 0.001 for the blue, green, and red bands). Moreover, the SSSI shows an RMSD of 0.0007 and the SEPM expresses an excellent RMSD around 0.5 dS.m^{-1} (electrical conductivity unit) reflecting a relative error that varies between 0.001 and 0.05, respectively, for salinity classes varying between 2.5 and 600 dS.m^{-1}. Likewise, the two used pairs of images exhibited very significant fits (R^2 of 0.93 for the costal and $R^2 \geq 0.96$ for the other bands of land surface reflectance, and R^2 of 0.95 for SSSI and SEPM). Excellent consistency was also observed between the derived products of the two sensors, yielding RMSD values less than 0.029 (reflectance units) for the bands and less than 0.004 for SSSI. While, the calculated RMSD for the SEPM fluctuate between 0.12 and 2.65 dS.m^{-1}, respectively, of non-saline and extreme salinity classes, which means that the relative errors varies between 0.005 and 0.03 for the considered soil salinity classes (i.e., between non-saline to extreme salinity). In general, independently to the used data (simulated or images) the statistical fits were found to be highly significant ($0.95 \leq R^2$) and the reached RMSD values (< 0.029) were smaller than the accuracy of radiometric calibration process (0.03) as demonstrated by Markham *et al.* [7]. Moreover, despite the small differences especially in coastal and blue

bands, the results of this research pointed out that MSI and OLI sensors can be combined for high temporal frequency to monitor soil salinity dynamic in time and space in an arid landscape. However, rigorous preprocessing issues such as sensors calibration, atmospheric corrections, and BRDF normalization must be addressed before the joint use of acquired data with these two sensors.

REFERENCES

[1] A. Dai, "Drought under global warming: A review," *WIREs Climate Change*, vol. 2, pp. 45–65, Jan./Feb. 2011.
[2] B. Kurylyk and K. MacQuarrie, "The uncertainty associated with estimating future groundwater recharge: A summary of recent research and an example from a small unconfined aquifer in a northern humid-continental climate," *J. Hydrol.*, vol. 492, pp. 244–253, 2013.
[3] S. Shahid and A. Al-Shankiti, "Sustainable food production in marginal lands-case of GDLA member countries," *Int. Soil Water Conservation Res.*, vol. 1, no. 1, pp. 24–38, 2013.
[4] S. Teh and H. Koh, "Climate change and soil salinization: Impact on agriculture, water and food security," *Int. J. Agriculture, Forestry Plantation*, vol. 2, pp. 1–9, 2016.
[5] O. A. Naing *et al.*, "Food security and socio-economic impacts of soil salinization in northeast thailand," *Int. J. Environmental Rural Develop.*, vol. 4, no. 2, pp. 76–81, 2013.
[6] R. White *et al.*, "An ecosystem approach to drylands: Building support for new development policies," World Res. Inst., WA, DC, USA, 2002, pp. 1–14.
[7] FAO, Rome, Italy, "Management of irrigation-induced salt-affected soils," 2005. [Online]. Available: http://www.fao.org/tempref/agl/agll/docs/salinity_brochure_eng.pdf
[8] G. I. Metternicht and J. A. Zinck, "Remote sensing of soil salinity: Potentials and constraints," *Remote Sens. Environ.*, vol. 85, pp. 1–20, 2003.
[9] H. Zhang, J. L. Schroder, J. J. Pittman, J. J. Wang, and M. E. Payton, "Soil salinity using saturated paste and 1:1 soil to water extracts," *Soil Sci. Soc. America J.*, vol. 69, pp. 1146–1151, 2005.
[10] G. I. Metternicht and J. A. Zinck, "Spatial discrimination of salt- and sodium-affected soil surfaces," *Int. J. Remote Sens.*, vol. 18, pp. 2571–2586, 1997.
[11] R. Goosens, M. El Badawi, and T. Ghabour, "De Dapper, M. A simulated model to monitor the soil salinity in irrigated arable land in arid areas based upon remote sensing and GIS," *EARSeL Adv. Remote Sens.*, vol. 2, pp. 165–171, 1998.
[12] A. Bannari, "Synergy between sentinel-msi and landsat-oli to support high temporal frequency for soil salinity monitoring in an arid landscape," in *Research Developments in Saline Agriculture*, J. C. Dagar, R. K. Yadav, and P. C. Sharma, Eds., Berlin, Germany: Springer, 2019, ch. 3, pp. 67–93,. [Online]. Available: https://doi.org/10.1007/978-981-13-5832-6_3
[13] A. Abuelgasim and R. Ammad, "Mapping soil salinity in arid and semi-arid regions using Landsat-8 OLI satellite data," *Remote Sens. Appl., Soc. Environ.*, vol. 13, pp. 425–425, 2018. [Online]. Available: https://doi.org/10.1016/j.rsase.2018.12.010
[14] A. B., A. El-Battay, R. Bannari, and H. Rhinane, "Sentinel-MSI VNIR and SWIR bands sensitivity analysis for soil salinity discrimination in an arid landscape," *Remote Sens.*, vol. 10, 2018, Art. no. 855.
[15] E. Ben-Dor *et al.*, "Review of remote sensing-based methods to assess soil salinity," in *Remote Sensing of Soil Salinization: Impact on Land Management*, G. Metternicht and J. A. Zinck, Eds., Boca Raton, FL, USA: CRC Press, 2009, ch. 13, pp. 39–60.

[16] S. Nawar, H. Buddenbaum, J. Hill, and J. Kozak, "Modeling and mapping of soil salinity with reflectance spectroscopy and landsat data using two quantitative methods (PLSR and MARS)," *Remote Sens.*, vol. 6, pp. 10813–10834, 2014.
[17] J. A. Zinck, "Monitoring soil salinity from remote sensing data," in *Proc. 1st Workshop EARSel Special Interest Group Remote Sens. Developing Countries*, Sep. 2000, pp. 359–368.
[18] E. Mandanici and G. Bitelli, "Preliminary comparison of sentinel-2 and landsat 8 imagery for a combined use," *Remote Sens.*, vol. 8, 2016, Art. no. 1014. doi:10.3390/rs8121014.
[19] D. P. Roy *et al.*, "Landsat-8: Science and product vision for terrestrial global change research," *Remote Sens. Environ.*, vol. 145, pp. 154–172, 2014. [Online]. Available: https://doi.org/10.1016/j.rse.2014.02.001
[20] M. A. Wulder *et al.*, "Virtual constellations for global terrestrial monitoring," *Remote Sens. Environ.*, vol. 170, pp. 62–76, 2015. [Online]. Available: https://doi.org/10.1016/j.rse.2015.09.001
[21] H. K. Zhang *et al.*, "Characterization of Sentinel-2A and Landsat-8 top of atmosphere, surface, and nadir BRDF adjusted reflectance and NDVI differences," *Remote Sens. Environ.*, vol. 215, pp. 482–494, Sep. 2018. [Online]. Available: https://doi.org/10.1016/j.rse.2018.04.031
[22] J. Hedley, C. Roelfsema, B. Koetz, and S. Phinn, "Capability of the Sentinel 2 mission for tropical coral reef mapping and coral bleaching detection," *Remote Sens. Environ.*, vol. 120, pp. 145–155, May 2012. [Online]. Available: https://doi.org/10.1016/j.rse.2011.06.028
[23] J. Li and D. P. Roy, "A global analysis of sentinel-2A, sentinel-2B and landsat-8 data revisit intervals and implications for terrestrial monitoring," *Remote Sens.*, vol. 9, 2017, Art. no. 902.
[24] M. Drusch *et al.*, "Sentinel-2: ESA's optical high-resolution mission for GMES operational services," *Remote Sens. Environ.*, vol. 120, pp. 25–36, May 2012. [Online]. Available: https://doi.org/10.1016/j.rse.2011.11.026
[25] J. R. Irons, J. L. Dwyer, and J. A. Barsi, "The next Landsat satellite: The Landsat data continuity mission," *Remote Sens. Environ.*, vol. 122, pp. 11–21, Jul. 2012. [Online]. Available: https://doi.org/10.1016/j.rse.2011.08.026
[26] N. Flood, "Comparing sentinel-2A and landsat 7 and 8 using surface reflectance over australia," *Remote Sens.*, vol. 9, 2017, Art. no. 659, doi: 10.3390/rs9070659 .
[27] B. Markham *et al.*, "Landsat-8 operational land imager radiometric calibration and stability," *Remote Sens.*, vol. 6, no. 12, pp. 12275–12308, 2014.
[28] E. F. Vermote, C. Justice, M. Claverie, and B. Franch, "Preliminary analysis of the performance of the Landsat 8/OLI land surface reflectance product," *Remote Sens. Environ.*, vol. 185, pp. 46–56, Nov. 2016. [Online]. Available: https://doi.org/10.1016/j.rse.2016.04.008
[29] D. P. Roy *et al.*, "Examination of Sentinel-2A multi-spectral instrument (MSI) reflectance anisotropy and the suitability of a general method to normalize MSI reflectance to nadir BRDF adjusted reflectance," *Remote Sens. Environ.*, vol. 199, pp. 25–38, Sep. 2017. [Online]. Available: https://doi.org/10.1016/j.rse.2017.06.019
[30] S. Skakun, J. C. Roger, E. F. Vermote, J. G. Masek, and C. O. Justice, "Automatic subpixel co-registration of Landsat-8 operational land imager and sentinel-2A multispectral instrument images using phase correlation and machine learning based mapping," *Int. J. Digital Earth*, vol. 10, pp. 1–17, 2017.
[31] L. Yan, D. P. Roy, Z. Li, H. K. Zhang, and H. Huang, "Sentinel-2A multitemporal misregistration characterization and an orbit-based sub-pixel registration methodology," *Remote Sens. Environ.*, vol. 215, pp. 495–506, Sep. 2018. [Online]. Available: https://doi.org/10.1016/j.rse.2018.04.021
[32] A. Bannari, P. M. Teillet, and R. Landry, "Comparison of natural surface reflectances in homologous spectral bands of TM and ETM+ sensors onboard Landsat-5 and Landsat-7," *Remote Sensing J.*, vol. 4, no. 3, pp. 263–275, 2004.
[33] H. Van-der-Werff and F. Van-der-Meer, "Sentinel-2A MSI and Landsat 8 OLI provide data continuity for geological remote sensing," *Remote Sens.*, vol. 8, 2016, Art. no. 883, doi:10.3390/rs8110883.
[34] R. P. Shrestha, "Relating soil electrical conductivity to remote sensing and other soil properties for assessing soil salinity in northeast Thailand," *Land Degradation Develop.*, vol. 17, pp. 677–689, 2006.
[35] A. Bannari, A. M. Guedon, and A. El-Ghmari, "Mapping slight and moderate saline soils in irrigated agricultural land using advanced land imager sensor (EO-1) data and semi-empirical models," *Commun. Soil Sci. Plant Anal.*, vol. 47, pp. 1883–1906, 2016.
[36] A. Bannari, A. El-Battay, N. Hameid, and F. Tashtoush, "salt-affected soil mapping in an arid environment using semi-empirical model and landsat-OLI data," *Adv. Remote Sens.*, vol. 6, pp. 260–291, 2017.

[37] A. Bannari *et al.*, "Potential of worldview-3 data for soil salinity modeling and mapping in an arid environment," in *Proc. Int. Geosci. Remote Sens. Symp.*, Jul. 2017, pp. 1585–1588.

[38] A. P. Leone *et al.*, "A field experiment on spectrometry of crop response to soil salinity," *Agricultural Water Manage.*, vol. 89, pp. 39–48, 2007.

[39] I. O. A. Odeh and A. Onus, "Spatial analysis of soil salinity and soil structural stability in a semiarid region of New South Wales, Australia," *Environ. Manage.*, vol. 42, pp. 265–278, 2008.

[40] T. T. Zhang *et al.*, "Using hyperspectral vegetation indices as a roxy to monitor soil salinity," *Ecological Indicators*, vol. 11, pp. 1552–1562, 2011, doi:10.1016/j.ecolind.2011.03.025.

[41] J. E. Chapman, D. A. Rothery, P. W. Francis, and A. Pontual, "Remote sensing of evaporite mineral zonation in salt flats (salars)," *Int. J. Remote Sens.*, vol. 10, pp. 245–255, 1989, doi:10.1080/01431168908903860.

[42] N. A. Drake, "Reflectance spectra of evaporite minerals (400–2500 nm): Applications for remote sensing," *Int. J. Remote Sens.*, vol. 16, pp. 55–71, 1995, doi:10.1080/01431169508954576.

[43] F. Hawari, "Spectroscopy of evaporates," *Per Mineral*, vol. 71, pp. 191–200, 2002.

[44] S. Nawar, H. Buddenbaum, and J. Hill, "digital mapping of soil properties using multivariate statistical analysis and aster data in an arid region," *Remote Sens.*, vol. 7, pp. 1181–1205, 2015, doi:10.3390/rs70201181.

[45] M. Rahmati and N. Hamzehpour, "Quantitative remote sensing of soil electrical conductivity using ETM+ and ground measured data," *Int. J. Remote Sens.*, vol. 38, pp. 123–140, 2017.

[46] *ASD Technical Guide*, 4th ed., ASD, Boulder, CO, USA, 1999. [Online]. Available: http://www.asdi.com/products-spectroradiometers.asp

[47] P. M. Teillet and R. Santer, "Terrain elevation and sensor altitude dependence in a semi-analytical atmospheric code," *Can. J. Remote Sens.*, vol. 17, pp. 36–44, 1991.

[48] N. A. Elagib and S. A. A. Abdu, "Climate variability and aridity in Bahrain," *J. Arid Environ.*, vol. 36, pp. 405–419, 1997.

[49] FAO "Bahrain: Geography, climate and population," 2015. [Online]. Available: http://www.fao.org/nr/water/aquastat/countries_regions/bahrain/index.stm

[50] C. Boonthaiiwai and P. Saenjan, "Food security and socio-economic impacts of soil salinization in northeast Thailand," *Int. J. Environ. Rural Dev.*, vol. 4, pp. 76–81, 2013.

[51] Soil Survey Laboratory Methods Manual, USDA-NRCS, WA, DC, USA, 2004 .

[52] D. B. Lobell and G. P. Asner, "Moisture effects on soil reflectance," *Soil Sci. Soc. Amer. J.*, vol. 66, pp. 722–727, 2002.

[53] J. Farifteh, F. Van der Meer, M. Van der Meijde, and C. Atzberger, "Spectral characteristics of salt-affected soils: A laboratory experiment," *Geoderma*, vol. 145, pp. 196–206, 2008.

[54] J. C. Doomkamp, D. Brunsden, and D. K. C. Jones, in *Geology, Geomorphology and Pedology of Bahrain*. Norwich, U.K.: Geo-Abstracts, Univ. East Anglia, 1980.

[55] R. D. Jackson *et al.*, "Hand-held radiometry," in *Agricultural Reviews and Manuals*, Phoenix, AZ, USA: U.S. Dept. Agriculture Sci. Educ. Admin., 1980.

[56] S. Sandmeier, C. Muller, B. Hosgood, and G. Andreoli, "Sensitivity analysis and quality assessment of laboratory brdf data," *Remote Sens. Environ.*, vol. 64, pp. 176–191, 1998.

[57] E. Ben-Dor, C. Ong, and I. C. Lau, "Reflectance measurements of soils in the laboratory: Standards and protocols," *Geoderma*, vol. 245–246, pp. 112–124, 2015.

[58] A. Bannari, P. M. Teillet, and G. Richardson, "Necessity of radiometric calibration and standardization of remote sensing data," *Canadian J. Remote Sensing*, vol. 25, pp. 45–59, 1999.

[59] P. M. Teillet, K. Staenz, and D. J. Williams, "Effects of spectral, spatial, and radiometric characteristics on remote sensing vegetation indices of forested regions," *Remote Sens. Environ.*, vol. 61, pp. 139–149, 1997.

[60] M. D. Steven, T. J. Malthus, F. Baret, H. Xu, and M. J. Chopping, Intercalibration of vegetation indices from different sensor systems," *Remote Sens. Environ.*, vol. 88, pp. 412–422, 2003.

[61] H. K. Zhang and D. P. Roy, "Computationally inexpensive Landsat 8 operational land imager (OLI) pan-sharpening," *Remote Sens.*, vol. 8, no. 3, 2016, Art. no. 180 .

[62] S. Li, S. Ganguly, J. L. Dungan, W. L. Wang, and R. R. Nemani, "Sentinel-2 MSI radiometric characterization and cross-calibration with landsat-8 OLI," *Adv. Remote Sens.*, vol. 6, pp. 147–159, 2017, doi: 10.4236/ars.2017.62011.

[63] M. A. Wulder *et al.*, "Current status of Landsat program, science, and applications," *Remote Sens. Environ.*, vol. 225, pp. 127–147, May 2019. [Online]. Available: https://doi.org/10.1016/j.rse.2019.02.015

[64] T. R. Loveland and J. L. Dwyer, "Landsat: Building a strong future," *Remote Sens. Environ.*, vol. 122, pp. 22–29, Jul. 2012. [Online]. Available: https://doi.org/10.1016/j.rse.2011.09.022

[65] M. A. Wulder *et al.*, "The global Landsat archive: Status, consolidation, and direction," *Remote Sens. Environ.*, vol. 185, pp. 271–283, 2015. [Online]. Available: http://dx.doi.org/10.1016/j.rse.2015.11.032

[66] D. Roy *et al.*, "A general method to normalize Landsat reflectance data to nadir BRDF adjusted reflectance," *Remote Sens. Environ.*, vol. 176, pp. 255–271, Apr. 2016. [Online]. Available: https://doi.org/10.1016/j.rse.2016.01.023

[67] NASA, "Landsat-8 Instruments," 2014. [Online]. Available: http://www.nasa.gov/mission_pages/landsat/spacecraft/index.html

[68] E. J. Knight and G. Kvaran, "Landsat-8 operational land imager design, characterization and performance," *Remote Sens.*, vol. 6, pp. 10286–10305, 2014. doi:10.3390/rs61110286.

[69] F. Gascon *et al.*, "Copernicus sentinel-2 calibration and products validation status," *Remote Sens.*, vol. 9, 2017, Art. no. 584. [Online]. Available: https://doi.org/10.3390/rs9060584

[70] A. Stumpf, D. Michéa, and J.-P. Malet, "Improved co-registration of sentinel-2 and landsat-8 imagery for earth surface motion measurements," *Remote Sens.*, vol. 10, 2018, Art. no. 160, doi: 10.3390/rs10020160.

[71] R. B. Myneni and G. Asrar, "Atmospheric effects and spectral vegetation indices," *Remote Sens. Environ.*, vol. 17, pp. 390–402, 1994. [Online]. Available: https://doi.org/10.1016/0034-4257(94)90106-6

[72] N. Pahlevan *et al.*, A. "On-orbit radiometric characterization of OLI (landsat-8) for applications in aquatic remote sensing," *Remote Sens. Environ.*, vol. 154, pp. 272–284, 2014. [Online]. Available: https://doi.org/10.1016/j.rse.2014.08.001

[73] P. M. Teillet, "an algorithm for the radiometric and atmospheric correction of AVHRR data in the solar reflective channels," *Remote Sens. Environ.*, vol. 41, pp. 185–195, 1992. [Online]. Available: https:/doi.org/10.1016/0034-4257(92)90077-W

[74] J. Qi, "Compositing multitemporal remote sensing data," Ph.D. dissertation, Dept. Soil Water Sci., Univ. Arizona, Tucson, AZ, USA1993.

[75] E. Scudiero, T. H. Skaggs, and D. L. Corwin, "Comparative regional-scale soil salinity assessment with near-ground apparent electrical conductivity and remote sensing canopy reflectance," *Ecological Indicators*, vol. 70, pp. 276–284, 2016.

[76] A. Bannari, A. M. Guedon, A. El-Harti, F. Z. Cherkaoui, and A. El-Ghmari, "Characterization of slight and moderate saline and sodic soils in irrigated agricultural land (Tadla, Morocco) using simulated data of ALI (EO-1) sensor," *J. Soil Sci. Plant Anal.*, vol. 39, pp. 2795–2811, 2008.

[77] X. W. Fan, Y. B. Liu, J. M. Tao, and Y. L. Weng, "Soil salinity retrieval from advanced multi-spectral sensor with partial least square regression," *Remote Sens.*, vol. 7, pp. 488–511, 2015.

[78] D. D. Alexakis, I. N. Daliakopoulos, L. S. Panagea, and I. K. Tsanis, "Assessing soil salinity using WorldView-2 multispectral images in Timpaki, Crete, Greece," *Geocarto Int.*, vol. 33, no. 4, pp. 321–338, 2016, doi: 10.1080/10106049.2016.1250826.

[79] A. El-Battay, A. Bannari, N. A. Hameid, and A. A. Abahussain, "Comparative study among different semi-empirical models for soil salinity prediction in an arid environment using OLI landsat-8 data," *Adv. Remote Sens.*, vol. 6, pp. 23–39, 2017.

[80] Z. Al-Ali, A. Bannari, N. Hameid, and A. El-Battay, "Physical models for soil salinity mapping over arid landscape using landsat-oli and field-soil sampling data: Validation and comparison," in *Proc. IEEE Int. Geosci. Remote Sens. Symp.*, 2019, pp. 7081–7084.

[81] H. Wu and A. Li, "Scale issues in remote sensing: A review on analysis, processing and modeling," *Sensors*, vol. 9, pp. 1768–1793, 2009, doi:10.3390/s90301768.

[82] C. J. Willmott, "Some comments on the evaluation of model performance," *Bull. Amer. Meteorol. Soc.*, vol. 63, pp. 1309–1313, 1982.

[83] J. D. Rhoades, F. Chanduvi, and S. Lesch, "Soil salinity assessment: Methods and interpretation of electrical conductivity measurements," FAO, Rome, Italy, Rep. no. 57, 1999. [Online]. Available: http://www.fao.org/docrep/019/x2002e/x2002e.pdf

[84] E. Davis, C. Wang, and K. Dow, "Comparing sentinel-2 MSI and landsat 8 OLI in soil salinity detection: A case study of agricultural lands in coastal North Carolina," *Int. J. Remote Sens.*, vol. 40, no. 16, pp. 6134–6153, 2019, doi: 10.1080/01431161.2019.1587205.

[85] N. J. Pastick, B. K. Wylie, and Z. Wu, "Spatiotemporal analysis of landsat-8 and sentinel-2 data to support monitoring of dryland ecosystems," *Remote Sens.*, vol. 10, 2018, Art. no. 791, doi: 10.3390/rs10050791.

[86] F. Vuolo *et al.*, "Data service platform for Sentinel-2 surface reflectance and value-added products: System use and examples," *Remote Sens.*, vol. 8, 2016, Art. no. 938.

[87] D. P. Roy *et al.*, "Landsat-8 and Sentinel-2 burned area mapping - A combined sensor multi-temporal change detection approach," *Remote Sens. Environ.*, vol. 231, 2019, Art. no. 111254. [Online]. Available: https://doi.org/10.1016/j.rse.2019.111254

Abdou Bannari received the B.Sc. degree in surveying engineering from the Agronomic Institute Hassan-II, Rabat, Morocco, in 1987, the M.Sc. degree in geomatic sciences from Laval University, Quebec City, QC, Canada, in 1989, and the Ph.D. degree in remote sensing form Sherbrooke University, Sherbrooke, QC, Canada, respectively, in 1996.

After his early retirement as a remote sensing Professor from the University of Ottawa, Ottawa, ON, Canada, he was acting as a Chair of the Department of Geoinformatics, Arabian Gulf University (AGU), Kingdom of Bahrain. He was a Visiting Scientist with SPAR Aerospace Limited, Montreal, QC, JPL-NASA, Pasadena, CA, USA, and Canada Centre for Remote Sensing Ottawa. He has authored two books and more than 220 articles, and he supervised more than 58 graduate students. Currently, he is running a private company "*Space Pix-Map International Inc.*," for international scientific consultations in remote sensing and Geomatics, Ottawa.

Nadir Hameid Mohamed Musa received the B.Sc. degree in geology from the University of Mousl, Mousl, Iraq, in 1988, the M.Sc. and Ph.D. degrees in geoinformatics from the University of Khartoum, Khartoum, Sudan, in 2006 and 2012, respectively.

He worked during many years for ministry of Agriculture in Sudan for information technology integration in natural resource applications. Since 2001 he holds a Geoinformatics specialist position with the Arabian Gulf University, Manama, Bahrain.

Abdelgadir Abuelgasim received the master's and Ph.D. degrees from Boston University, Boston, MA, USA, in 1992 and 1996, respectively.

He worked for one year as an Assistant Professor of remote sensing and surveying with Sultan Qabous University, Oman. He later joined NASA Goddard Space Flight Center, Maryland, USA, in 1998 as a Visiting Scientist. In 2000, he relocated to Canada where he has been with the Canada Centre for Remote Sensing and the Canadian Space Agency as a Research Scientist. He is currently an Associate Professor with the Department of Geography and Urban Sustainability, United Arab Emirates University, Al Ain, UAE. His research and teaching interests include the analysis of geospatial data for information products generation, physical and human geography, hydrology, and on the effects of human induced environmental and ecological changes.

Ali El-Battay received the B.Sc. degree in environmental studies from University Hassan-II, Mohammedia, Morocco, in 1998, the M.Sc. and Ph.D. degrees in remote sensing from INRS-Eau, Quebec City, QC, Canada, in 2001 and 2006, respectively.

He is a Senior Scientist—Remote Sensing and Drones Technology—with the International Center for Biosaline Agriculture, Dubai, UAE. Concurrently, he is the Chief Innovation Officer at the first established and leading drones solutions company in Dubai; Falcon Eye Drones. Before that, he was an Assistant and Associate Professor, respectively, with the *Universiti Teknologi Malaysia* (Malaysia) and the Arabian Gulf University, Bahrain.